# ARCHER

*Collaborative Project*

Co-funded by the European Commission under the
Euratom Research and Training Programme on Nuclear Energy
within the Seventh Framework Programme

Grant Agreement Number: 269892
Start date: 01/02/2011 Duration: 48 Months

*www.archer-project.eu*

# D23.42 - Experimental Results on Dust Remobilization in Pebble Bed Structures

Authors: Thomas Barth (HZDR), Uwe Hampel (HZDR)

**ARCHER project** – Contract Number: 269892
Advanced High-Temperature Reactors for Cogeneration of Heat and Electricity R&D
EC Scientific Officer: Dr. Panagiotis Manolatos

| | |
|---|---|
| Document title | Experimental Results on Dust Remobilization in Pebble Bed Structures |
| Author(s) | Thomas Barth (HZDR), Uwe Hampel (HZDR) |
| Number of pages | 17 |
| Document type | Deliverable |
| Work Package | WP23 |
| Document number | D23.42 – revision 0 |
| Issued by | HZDR |
| Date of completion | 18/01/2013 |
| Dissemination level | Restricted to the partners of the ARCHER project |

**Summary**

The particle deposition and resuspension was studied in a pebble bed. A small-scale test facility called Pebble Bed Loop (PBLoop) was designed to generate a particle laden turbulent flow through a pebble bed. The dimensions of the facility were fluid dynamically scaled to match the characteristic numbers related to the flow field in a pebble bed core of a High Temperature Reactor (HTR). Results of pressure drop and velocity measurements are presented for the quantification of the turbulent flow field. The comparison of the total pressure drop over the pebble bed demonstrates the correct scaling of the pebble bed. Furthermore, particle number and mass concentration measurements over the pebble bed were performed to determine overall the particle deposition behaviour. Considering the present Reynolds numbers and particle relaxation times it was found that the particle deposition process is mainly driven by turbulent dispersion and particle inertia.

The aerosol particles were radioactively labelled with the isotope fluorine 18 and the spatiotemporal distribution of the particles was recorded by means of Positron Emission Tomography (PET). Two sets of experiments were conducted. In the first phase, monodisperse liquid aerosol particles were injected into the flow field far upstream of the pebble bed to study pure particle deposition. The influence of particle size and fluid velocity were systematically investigated. In the second phase, the liquid particles were replaced with technical graphite dust. The graphite dust was injected into the loop at moderately low fluid velocities to study the deposition process. After the entire activity was dispersed the aerosol generator was switched off and particle resuspension was caused by the stepwise increase of the fluid velocity. The PET scanner online recorded the remobilisation of the graphite dust by the instant drop of the count rates indicating the fraction of resupended material.

This report gives a general overview of the experimental results and the findings emanating from the conducted particle transport experiments in the pebble bed.

**Approval**

| Rev. | Short description | First author | WP Leader | SP leader | Coordinator |
|---|---|---|---|---|---|
| 0 | First issue | T Barth (HZDR) | K Verfondern | N Kohtz | S deGroot (NRG) |

**Distribution list**

| Name | Organisation | Comments |
|---|---|---|
| P. Manolatos | EC DG RTD | |
| All technical participants | ARCHER | |
| Steering Committee members | ARCHER | |

**Table of contents**

# 1 Boundary conditions of the two sets of experiments

The entire campaign was split into two sets of experiments. Firstly, the pebble bed was made of hollow polypropylene spheres to reduce the attenuation of the gamma radiation. Thereby, the required initial activity was substantially reduced at which PET image reconstruction is still meaningful. In the second phase, the plastic spheres were replaced with hollow graphite spheres to get closer to the material composition of the HTR pebble bed. Furthermore, electrostatic effects were removed by using electrically conductive graphite spheres instead of polypropylene spheres. The axial length of the pebble bed was reduced from *4* to *2* tube diameters in order to reduce the scatter radiation originating from deposited activity outside of the field of view (FOV). Table 1 gives an overview of the geometric specifications.
In addition, the power unit of the PBLoop was upgraded from *1* to *2* radial fans to extend the operational range of the PBLoop as noted in Table 1. The power upgrade was necessary to allocate sufficient fluid and friction velocities to study particle resuspension in the pebble bed.

Table 1 Specifications and boundary conditions of the two sets of experiments

| | First experimental phase | Second experimental phase |
|---|---|---|
| | Polypropylene spheres | Graphite spheres |
| Snapshot and CT image of the pebble bed |  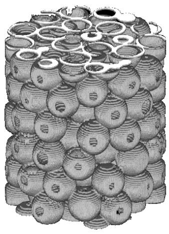 |  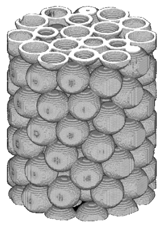 |
| $d_{pb}$ [mm] | 38 | 40 |
| $D/d_{pb}$ | 5.1 | 4.85 |
| ε | 0.41 | 0.51 |
| $L_{pb}$ | 4D | 2D |
| Number of radial fans | 1 | 2 |
| $v_{pb}$ [m/s] | 0.36 – 3.59 | 0.41 – 4.0 |
| $v_{pb}$* [m/s] | 0.06 – 0.40 | 0.06 – 0.45 |
| $Re_{pb}$' [-] | 220 – 2200 | 270 – 2640 |
| Particles | DEHS droplets | Graphite dust |
| $d_{Aero}$ [µm] | 1.5 – 3.5 | 0.5 - 20 |

In the first phase, liquid particles made of DEHS (Di-Ethyl-Hexyl-Sebacat) were used to study the pure particle deposition process in the pebble bed. The particles were generated by means of a condensational aerosol generator (SLG 270, TOPAS GmbH) and the condensation nuclei were labeled with the radioisotope fluorine 18 ($^{18}F$). In the second phase, technical graphite dust (23061, Thielmann Graphite GmbH) was dispersed into the PBLoop using a solid aerosol generator (SAG 410, TOPAS GmbH).

# 2 Particle characterization and radioactive labelling

The particle size is characterized by the aerodynamic particle size distributions, which were measured by an Aerodynamic Particle Sizer (APS 3321, TSI Inc) Spectrometer as shown in Figure 1. The histogram on the left hand side displays the three particle size distributions provided by the condensational aerosol generator (SLG 270). The volume related geometric standard distribution of the three particle classes is smaller than $\sigma_g < 1.15$ whereupon the particles are denoted as monodisperse.

Ziermann and Ivens (1997) and Rott and Wahsweiler (1991) reported about the particle size distribution found in the primary circuit of the AVR and the THTR. The dust was analysed from hot gas filter experiments using scanning electron microscopy. The particle size distributions are displayed in the plot on the right hand side. In the THTR, the dust was sampled at different side locations. The dotted line (THTR) represents the particle size distribution obtained from sampling at the humidity detectors. The solid line (cyclone) shows the size distribution originating from a sample taken downstream of a cyclone. Thus, the size distribution is shifted to larger particles. Furthermore, the dust was milled to break up particle agglomerates (crushing).

Note, the AVR seems to have a one order of magnitude smaller particle size distribution compared to the THTR dust. Ziermann and Ivens (1997) mention the influence of particle agglomeration while it is unsure whether this process took place before or after particle sampling. Note, the dust in the AVR has a date of origin of about $20$ years whereas the THTR dust had an age of about two years. It is assumed that the AVR dust size distribution might have changed during reactor operation due to milling processes and particle breakup. Since there is no further information available about the aerodynamic particle size distribution of the AVR and THTR dust we decided to use a technical graphite dust (Präzisionsgraphit 23061, Thielmann Graphite), which is in between the two particle size distributions. The material has an unimodal distribution with a volume averaged aerodynamic particle diameter of about $5.6\ \mu m$.

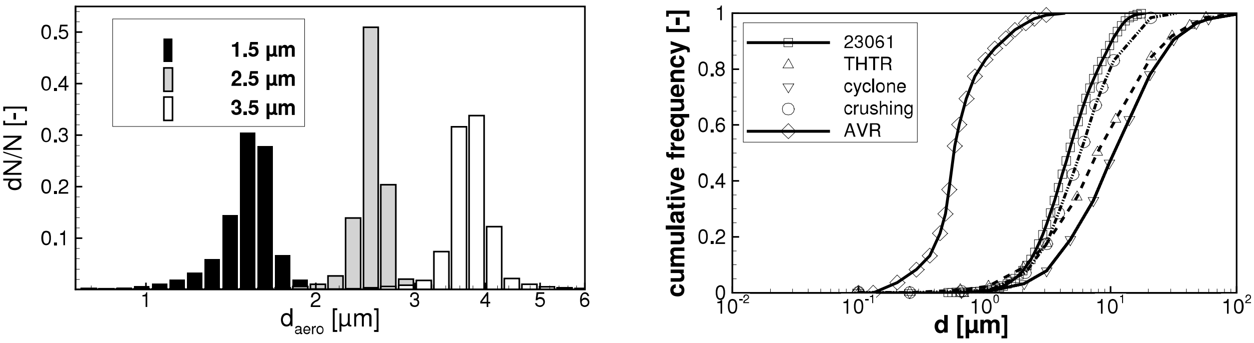


Figure 1 Aerodynamic particle size distritions, left : liquid DEHS particles, right : 23061 graphite dust

The radioactive labelling process of the liquid particles was performed by marking the condensation nuclei with $^{18}F$ as further described in the ARCHER report D23.41. The labelling of the graphite particles was performed differently. The activity allocated by the cyclotron is usually provided in a solution of distilled water. Dispersing humidity into a dry powder leads to agglomeration and in consequence to a change of the particle size distribution. In order to dispense the activity homogeneously on the graphite particles the initial solution was diluted with additional $50\ ml$ distilled water. This solution was mixed into the graphite dust which was dispersed into the PBLoop flow field afterwards. In order to conserve the original characteristics of the graphite particles the activated dust had to be dried before being dispersed into the flow field. The drying process was performed in a heating furnace at a temperature below the auto ignition temperature of graphite dust. In order to assess the required drying time of $10\ g$ graphite dust dissolved in $50\ ml$ the mixture was placed in the heating furnace and the residual mass of the sample was weighed every $5\ minutes$. Figure 2 displays the time evolution in terms of the ratio between the actual mass $m_1$ and the initial mass $m_0$ at $t = 0\ min$ under variation of the average temperature in the heating furnace. All curves show a decreasing slope over time because the water evaporated out of the graphite water mixture. The mass ratios at the temperatures $200\ °C$ and $250\ °C$ still show a decreasing tendency after $40\ minutes$. In contrast, the mass ratios at $300\ °C$ and $350\ °C$ reach a constant level after $45$ and $30\ minutes$. Thus, the labelled dust is dried for about $35\ min$ at $350\ °C$ before injection into the PBLoop flow field.

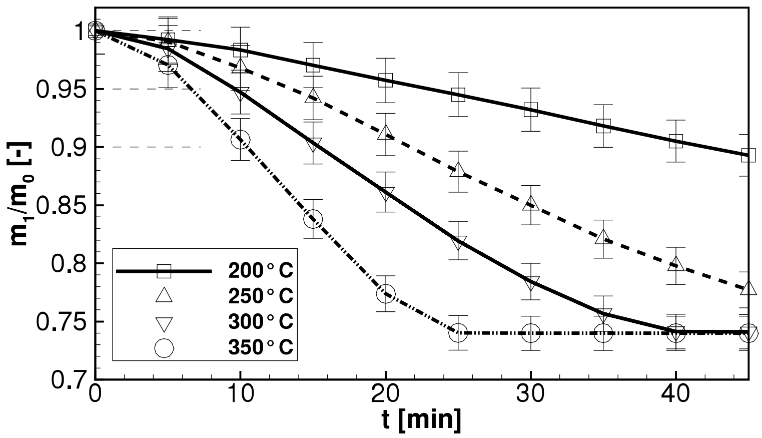


Figure 2 Mass ratio of the graphite dust sample against time during drying process

The particle size distribution of the dried graphite dust was rechecked by an aerodynamic particle sizer spectrometer (APS 3321) and it was found that the drying process had no influence on the original particle size distribution. The efficiency of the labelling process was evaluated by comparing the activity provided by the cyclotron with the decay corrected activity of the labelled graphite dust after the drying routine. The dust was placed in an activimeter before dispersion into the PBLoop. It turns out that $50\%$ to $62\%$ of the initial activity remained in the dust. The residual activity has probably left the dust sample with the water vapour.

# 3 Fluid dynamic instrumentation of the test section

The test section was equipped with Pitot tube shaped sampling nozzles and wall static pressure ports in order to measure different fluid dynamic parameters. The general arrangement is displayed in Figure 3. Following Truckenbrodt (2008) the dynamic pressure corresponding to the fluid velocity in midsection is the difference between the total pressure (Pitot tube) and the wall static pressure (wall static pressure port). This pressure difference was measured by an inclined tube manometer. Furthermore, the total pressure drop over the pebble bed was determined out of the static pressure difference upstream and downstream of the pebble bed. The measurement uncertainty of the inclined tube manometer is about $15\%$ of the pressure signal.

Particle concentration measurements were performed by the isokinetic sampling technique further described in Vincent (2007) at the measurement side locations $2$ and $3$. In the first phase of the experiment the particle number concentration of the liquid particles was recorded using a condensational particle counter (UCPC 3025A, TSI Inc.). According to Farnsworth and Caldow (2010) the collection efficiency of the UCPC is larger than $90\%$ for particles smaller than $4\ \mu m$ in aerodynamic diameter. Thus, the measurement uncertainty of the particle number concentration is about $10\%$. In the second phase, the particle counter was replaced with an out-stack filter sampling system to measure the overall graphite mass concentration. A graphite particle laden air sample was removed isokinetically out of the flow and the particles were collected on a pore filter. The airborne mass concentration was calculated out of the mass collected by the filter divided by the sampled fluid volume. Since this procedure has more sources of errors (determination of the sampled mass by scaling, sampled volume, etc.) in comparison to the online monitoring by the UCPC the overall measurement uncertainty accounts up to $25\%$.

Furthermore the out-stack filter system was replaced with an APS 3321 to measure the aerodynamic particle size distribution of the graphite particles with respect to different drying temperatures.

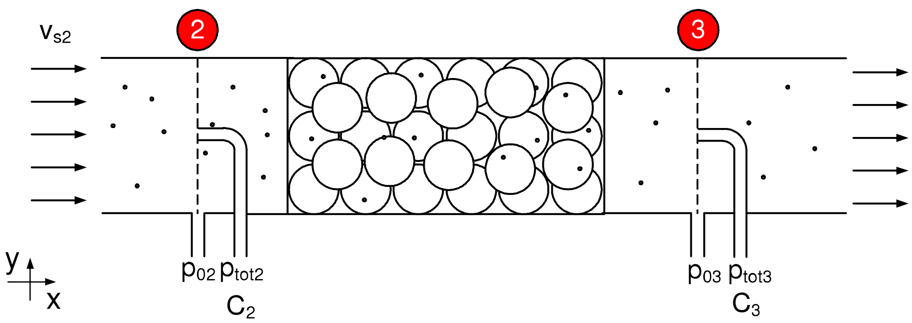


Figure 3 Fluid dynamic instrumentation of the test section, 2 and 3 denote the side locations upstream and downstream of the pebble bed

# 4 Experimental results

## 4.1 The turbulent flow field

The fluid velocities were measured at the side locations as marked in Figure 1 of the ARCHER deliverable D23.41. It turns out that the most accurate determination of the fluid velocity and the volume flow rates are achieved at a side location with a sufficient flow field development and minimum pipe diameter. These conditions are fulfilled at best at side location *1* because the flow has already passed a *7* hydraulic diameter long straight pipe section and the inner diameter is about $d_1 = 100\ mm$. The superficial velocity of the empty tube holding the pebble bed is computed according to volume continuity after

$$v_{spb} = \frac{(d_1 / D)^2 \cdot v_1}{1.25}, \qquad (4\text{-}1)$$

where $D$ is the inner diameter of the pipe containing the pebble bed. The factor *1.25* in the denominator has been chosen because the velocity seen by the Pitot tube in the channel centre is the maximum velocity. The mean velocity within the pebble bed is computed by dividing $v_{spb}$ by the pebble bed porosity $\varepsilon$ according to $v_{pb} = v_{spb}/\varepsilon$. In order to compare the present results of the total pressure drop over the pebble bed the modified Reynolds number of pebble bed $Re_{pb}$‘ is introduced according to the definition of Eisfeld and Schnitzlein (2001)

$$\mathrm{Re}'_{pb} = \mathrm{Re}_{pb} \cdot (1-\varepsilon) = \frac{v_{spb} \cdot d_{pb}}{\nu_{air}} \cdot (1-\varepsilon), \qquad (4\text{-}2)$$

where $\nu_{air}$ is the kinematic viscosity of air at ambient conditions. In addition, the average friction velocity over the pebble bed was computed out of the Reynolds number and the maximum velocity in the pebble bed following the formula of Pope (2009)

$$v^*_{pb} = \frac{v_{pb\max}}{5 \cdot \log_{10}(\mathrm{Re}_{pb})}. \qquad (4\text{-}3)$$

According to Truckenbrodt (2008) the ratio of the maximum velocity to the mean velocity in a fully developed turbulent pipe flow is approximately *1.2*. Since the flow in a pebble bed has to pass much larger surface areas through much smaller interspaces it is assumed that frictional and viscous effects may increase this velocity ratio considerably. The first guess for the present study is a velocity ratio in the pebble bed of about *2*. The results of these measurements are listed in Table 1, respectively.

The correct downscaling of the flow field was studied by comparing the non-dimensional pressure drop according to the notation of Eisfeld and Schnitzlein (2001)

$$\Psi' = \frac{\Delta p_{pb} \cdot d_{pb} \cdot \varepsilon^3}{\rho_{air} \cdot v_{pb}^{\ 2} \cdot L_{pb}(1-\varepsilon)}. \qquad (4\text{-}4)$$

$\Delta p_{pb}$ is the measured static pressure difference between side location *2* and *3*, $\rho_{air}$ is the fluid density and $L_{pb}$ is the axial length of the pebble bed. The pressure drop measurements were performed for the polypropylene pebble bed with a length of about $L_{pb} = 80\ cm$.

Figure 4 shows the comparison between the present data and the results of Eisfeld and Schnitzlein (2001). There is a considerable deviation for a Reynolds number smaller than $Re_{pb}' < 1200$, but for larger values the decreasing slope is captured well by the present data. Thus, the fluid dynamic conditions are assumed to be similar the ones found in the HTR pebble bed. Note, the wall influence might be larger in the PBLoop because the tube-to-pebble diameter in a real HTR pebble bed core is up to one order of magnitude larger.

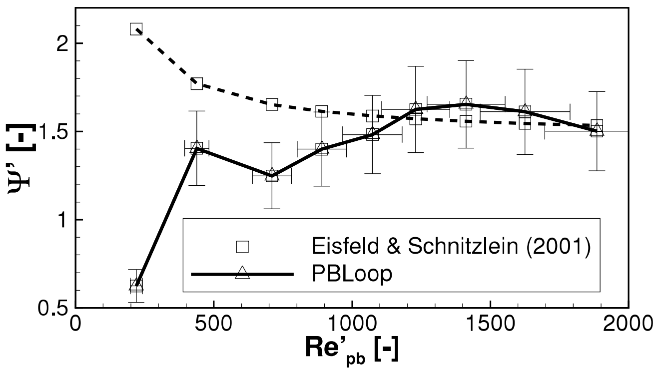


Figure 4 Non-dimensional pressure drop versus modified pebble bed Reynolds number

## 4.2 Particle number and mass concentration

Particle concentration measurements were performed at the measurement side locations 2 and 3 by means of the isokinetic sampling technique as further described by Vincent (2007). In the first set of experiments the fraction deposited of the liquid particles $\Delta C$ was calculated on the basis of the particle number concentration upstream and downstream of the pebble bed, $C_2$ and $C_3$, according to

$$\Delta C = \frac{(C_2 - C_3)}{C_2}. \quad (4\text{-}5)$$

The results are shown in Figure 5 as a function of the non-dimensional particle relaxation time $\tau^+$. The non-dimensional particle relaxation time is defined according to Tian & Ahmadi (2007) as

$$\tau^+ = \frac{\frac{\rho_{aerosol}}{\rho_{air}} \cdot d_{aero} \cdot {v^*_{pb}}^2}{18 \cdot \nu_{air}} Q. \quad (4\text{-}6)$$

Here $\rho_{aerosol}/\rho_{air}$ is the particle-to-fluid density ratio, $d_{aero}$ is the aerodynamic particle diameter, $v^*_{pb}$ is the mean friction velocity in the pebble bed, $Q$ is the Cunningham slip correction factor, which is set to unity.
The smallest particles used in our experiments ($d_{aero} = 1.5\ \mu m$) tend to deposit inside the pebble bed with an efficiency of about $\Delta C = 20\%$ and less. But with increasing particle size and fluid velocity (increasing particle relaxation time) the fraction deposited increases up to $\Delta C = 75\%$. It is assumed that the small particles have sufficiently high aerodynamic mobility for easy passing the pebble bed whereas the larger particles tend to deposit due to an increase of turbulent dispersion and particle inertia. Several authors - such as Peters and Leith (2004) - investigated particle deposition in curved geometries and also observed an increase of particle deposition with increasing particle inertia. This is expressed in terms of an s-shaped deposition curve, which can also be found in the present results. Thus, it is assumed that the particle deposition is mainly driven by turbulent dispersion and inertia impaction. In contrast, Hassan and Dominguez-Ontiveros (2008) observed an increase of particle deposition rates with respect to the pebble bed Reynolds number. Regarding the present findings it can be assumed that the deposition process in a pebble bed is rather related to the particle inertia and not to the pebble bed Reynolds number.

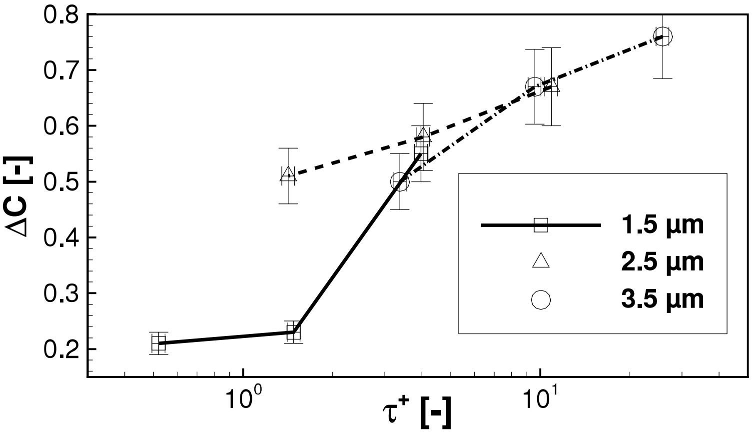


Figure 5 fraction deposited along the pebble bed vs. particle relaxation time

The mass concentration of the graphite particles was determined by isokinetic sampling in combination with an out-stack filtration system. Measurements were performed at the measurements side locations 2 and 3. The dispersion rate of the aerosol generator was set to maximum corresponding to a graphite particle mass flow rate of about $\Delta m/\Delta t = 18.5\ g/h$. The fluid velocity was adjusted to rather low Reynolds numbers ($Re_{pb}' < 578$) to a pure deposition regime. At larger fluid velocity the concentration values downstream of the pebble bed showed a considerable scatter, sometimes exceeding the values measured upstream of the pebble bed. Hence, particle resuspension is assumed to begin for Reynolds numbers larger than $Re_{pb}' > 578$, which was also observed by the time-resolved PET data during a resuspension experiment (chapter 5). To summarize, the fluid velocities and the particle mass concentrations are listed in Table 2.

Table 2 Fluid velocities and mass concentrations during the graphite deposition regime

| $Re_{pb}$' [-] | $v_{pb}$ [m/s] | $C_2$ [g/m³] | $C_3$ [g/m³] | $\Delta C$ [%] | $\Delta m/\Delta t_{pb}$ [g/h] |
|---|---|---|---|---|---|
| 273 | 0.41 | 257 | 186 | 28 | 1.6 |
| 587 | 0.87 | 139 | 111 | 20 | 1.3 |

# 5 PET and CT data processing

In the present study the PET scanner ClearPET was used. During the experiment the PET scanner records gamma radiation originating from annihilation events of positrons. Radionuclides used for PET undergo $\beta^+$ decay and emit such positrons. These positrons travel a short distance in the order of *1 mm* depending on the penetrated material until they annihilate with electrons (Levin & Hoffman, 1999). When a positron annihilates with an electron two photons with an energy of about $E_\gamma = 511\ keV$ each are emitted back-to-back. After passing through the object of investigation (in our case the pebble bed) and eventually interacting with its matter (Compton scatter and attenuation) a small fraction of these photons reach the detector system of the PET scanner. Whenever two detectors coincidentally register a photon interaction, this can be associated with an annihilation event. The detector positions in space then define the end-points of a so called line-of-response (LOR). The acquisition of millions of such LORs statistically allows to reconstruct the three-dimensional activity distribution in the field of view (FOV) by means of the OSMAPOSL algorithm from the open source reconstruction library STIR (Thielemans *et al.*, 2012).

The PET scanner consists of *20* detector modules arranged in a circle around the field of view as further described by Sempere-Roldan *et al.* (2006). The diameter of the FOV, where the activity distribution can be reliably reconstructed, is *163 mm* and thus somewhat below the internal diameter of the pebble bed. Common practice of PET data processing includes a number of procedures for correcting random coincidences, dead-time effects, absorption and scattering of annihilation photons, inhomogeneities caused by individual detector efficiencies and geometrical conditions, and calibration (Phelps, 2006). Here, we skip the material dependent corrections (absorption and scattering), because the bulk density of the material and thus its effective cross-section is low, and absorption and scattering corrections would increase the noise level. We just determined the rate of true coincidences $Tr$ by applying the random correction.

The time evolution of the particle deposits in the pebble bed is expressed in terms of true coincidences $Tr$ of the PET scanner. Assuming a mass related homogeneous distribution of the initial activity over the particles the measured activity recorded by the PET scanner directly correlates to the amount of deposited particles in the FOV. The true coincidences $Tr$ are expressed in terms of decay and background corrected total trues $Tr_{corr}$ according to

$$Tr_{corr}(t) = (Tr_{raw} - Tr_{Bkg}) \cdot e^{\frac{t \cdot \ln 2}{t_{0.5}}} \quad . \qquad (5\text{-}1)$$

$Tr_{raw}$ is the raw count rate, $Tr_{Bkg}$ is the count rate due to the background activity of the laboratory and $t_{0.5}$ is the half-life of the isotope fluorine 18 ($^{18}F$). The decay correction was performed to sum up the entire activity related to the overall value of the deposited particles. Note, the experiment lasted up to 6 hours which is approximately 3 times the half-life of $^{18}F$.

Apart from the constant background radiation effect ($Tr_{Bkg}$= *130 Coinc/s* for the liquid particles and $Tr_{Bkg}$= *320 Coinc/s* for the graphite particle experiment), which is mainly caused by the radioactivity of the detector crystals there is an additional background level, which originates from the high activity in the laboratory environment and has to be accounted for.

The 3D geometry of the pebble bed was obtained from a gamma ray computed tomography (CT) scan. The scanner used for this purpose has a spatial resolution of *2 mm* (Hampel *et al.*, 2007). The 3D volume was synthesized from *400* slice images obtained by vertical translation of the pebble bed (images of Table 1). Regarding the first set of PET experiments (liquid particle deposition) the better part of the activity initially fed into the aerosol generator was retained in the flow paths of the condensational aerosol generator. Only a small portion deposits on the pebbles in the field of view of the positron camera and the residual fraction finally gets adsorbed in the HEPA filter downstream of the pebble bed. Consequently, the signal-to-noise ratio (SNR) of the detected coincidences was rather low. One effect of low SNR is the appearance of ring artefacts in the reconstructed PET images, when filtered backprojection techniques are used for reconstruction. Furthermore, the free path length of the positrons in air prior to their annihilation amounts up to some millimetres causing a considerable fraction of the annihilation events to take place somewhat away from the pebble surfaces.

In order to increase the SNR of the first PET measurement campaign the gamma CT data of the polypropylene pebble bed was used as mask for the data analysis. Assuming all particles are distributed on the outer pebble surfaces the measured activity must also be distributed on the pebble surfaces. Reconstructed events in the interspaces of the pebbles can be referred as image artefacts. Thus, the gamma CT data was binarized by threshold binarization setting all voxels belonging to the extended pebble walls to *1* and all interspaces to *0*. This data set was fitted onto the reconstructed PET data to blank the events referred to the pebble interspaces. The resulting PET/CT image overlay is significantly clear from artefacts and noise and represents the recorded activity close to the pebble surfaces.

# 6 Time evolution of the PET experiments

## 6.1 Time evolution of the entire experiment

The time development of the first experiment (oil particles, polypropylene pebbles) is shown in Figure 6 with respect to two different initial activities, particle sizes and fluid velocities as further specified in Table 3.

Table 3 Boundary conditions of the liquid particle deposition experiment

| $A_{initial}$ [MBq] | $d_{aero}$ [µm] | $v_{pb}$ [m/s] | $Re_{pb}$' [-] |
|---|---|---|---|
| 709 | 3.5 | 2.3 | 1400 |
| 2020 | 3.5 | 3.6 | 2200 |

The slope can be subdivided into two parts. First, there is a flow regime in which the radioactive particles were continuously dispersed into the turbulent flow field. The corrected count rates show a linear trend against time. Hence, the particle deposition rate in the pebble bed is constant. After the entire activity was dispersed the aerosol generator and the radial fan was switched off. The PET scanner took a static image, in which the corrected count rate remains on a constant plateau.

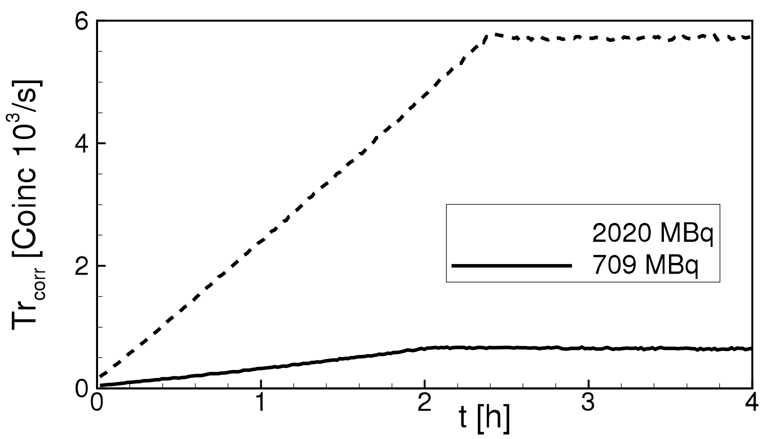


Figure 6 Temporal evolutions of the decay and background correct True count rates for a deposition experiment with liquid particles

The time evolution of the graphite experiment is somewhat different to the first campaign. Figure 7 shows the corrected count rates for two representative experiments. The entire campaign can be subdivided into 5 different phases according to the operation of the aerosol generator and the power unit. In the first phase denoted as “1” in Figure 7, the radial fan is set to a rather low fluid velocity ($Re_{pb}$' = *273* and *578*) corresponding to a pure deposition regime. The aerosol generator disperses the activated graphite dust with a constant mass flow rate of about *18.5 g/h* and the count rate $Tr_{corr}$ shows a linear slope against time. Likewise to the deposition phase of liquid particles the mass flow rate of graphite dust into the pebble bed seems to follow a linear tendency.
In the second phase, the settings of the power unit and the aerosol generator remain constant but the dispersion rate provided by the aerosol generator starts to become discontinuous. This can be related to the dispersion unit of the aerosol generator which consists of a rabble rake and a rotating ring. When the reservoir of the solid aerosol generator is almost empty the rabble rake does not bank the graphite particles continuously anymore. In consequence the mass concentration in the PBLoop and the deposition rate into the pebble bed decreases which results in a decline in the slope of the count rates $Tr_{corr}$. In the third phase, the aerosol generator is switched off (and remains off for the rest of the campaign) but the power unit

remains at the initial level. The count rates $Tr_{corr}$ increase during this part for about 10% which is related to particle resuspension between the particle injection and the pebble bed. It is assumed that a small graphite particle fraction deposited in the piping system upstream of the pebble bed was resuspended and deposited in the pebble bed.
During the fourth phase of the experiment the fan speed was stepwise increased beginning at the initial fan power level up to maximum power. During the experiment corresponding to $Re_{pb}' = 578$ the fan speed was directly increased up to maximum fan speed. The count rates $Tr_{corr}$ drops down from 23100 to 9650 Coinc/s. Assuming a homogeneous distribution of the activity on the graphite particle mass it can be assumed that approximately 58% of the graphite particles were resuspended during this scenario. Regarding the deposition regime performed at $Re_{pb}' = 273$ the count rates changed from 20800 to 7800 Coinc/s, which corresponds to a reduction of the activity in the pebble bed of about 62%. A detailed view on the resuspension scenario is given in chapter 6.2.
In the beginning of the fifth phase of the experiment the power unit was switched off and the PET scanner took a long term image. Since the entire periphery was off the convective transport of the aerosol particles decreases to zero. The corrected count rates $Tr_{corr}$ remain on a constant level since the remaining graphite dust in the pebble bed remains in a steady state.

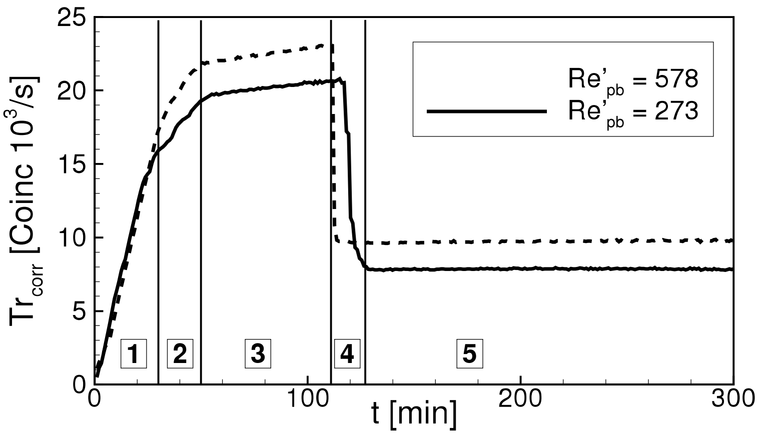


Figure 7 Temporal evolution of the count rates for a graphite experiment at two different Reynolds numbers

## 6.2 Time evolution during the resuspension scenario

The resuspension scenario labelled as “4” in Figure 7 is further considered by increasing the time resolution of the recorded count rates. After the deposition phase at $Re_{pb}' = 273$ the fan speed was stepwise increased every two minutes up to maximum power corresponding to a Reynolds number $Re_{pb}' = 2640$.
Firstly, the corrected count rates were determined each minute. Since the activity in the FOV is sufficiently high the time step of the count rates could be reduced down to one second. Figure 8 gives a detailed view on the resuspension scenario. Beginning with an increase of the friction velocity from $v_{pb}^* = 0.06$ m/s to 0.11 m/s there is almost no change in the count rates obvious. Following the count rates at higher friction velocities the largest reduction of the count rates can be seen between 0.11 and 0.20 m/s as well as between 0.20 and 0.28 m/s. Thus, it can be concluded that the bulk of the graphite particles tends to resuspend at a friction velocity range between $v_{pb}^* = 0.11$ and 0.30 m/s. By further increasing the friction velocity up to $v_{pb}^* = 0.43$ m/s the corrected count rates approach approximately 40% of the initial level of the corrected count rates at $t = 115$ min. Considering the minute resolved slope of the count rates each increase of the friction velocity is accompanied by a decreasing ramp and a plateau. However, the slope of the second resolved count rates shows the approaching of the corrected count rates already after 15 to 20 seconds (Figure 8, right). During the stepwise increase the radial fans of the PBLoop approximately needed 15 to 20 seconds until the flow field reached steady state condition, which is in the same temporal order of magnitude as the change of the corrected count rates. Thus, it is assumed that particle resuspension directly takes place when the local friction velocities exceed the required threshold value. Reeks and Hall (2001) performed a numerical study about particle resuspension. One of their findings was that most of resuspension takes places in the millisecond range. After one second at constant flow conditions the resuspension rate has already decreased for about 8 orders of magnitude. The count rates during the resuspension scenario also follow this immediate character of particle resuspension.

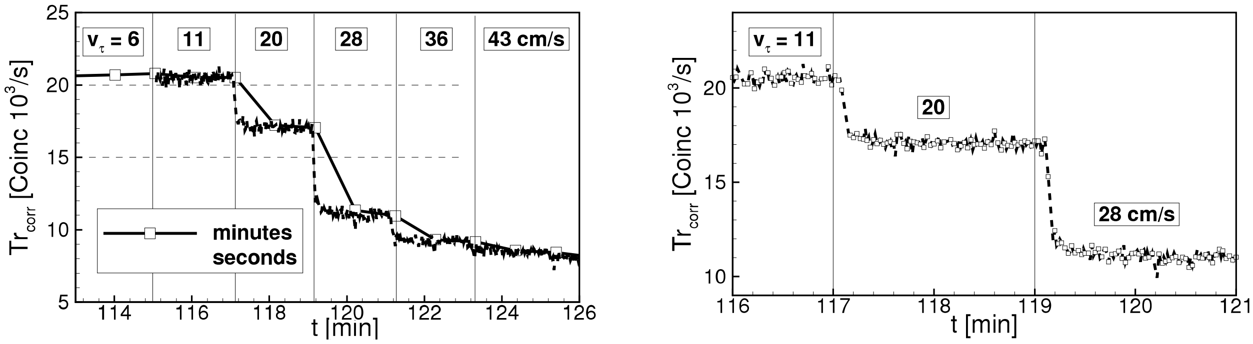


Figure 8 Time evolution of the corrected count rates during particle resuspension

For further quantification of the present resuspension process the corrected count rates $Tr_{corr}$ were normalized by the initial count rates $Tr_{corr}$ $(t = 115\ min)$ corresponding to the beginning of the resuspension scenario. Assuming homogeneous labelling of the graphite mass this ratio $Tr_{corr}(t)/Tr_{corr}(t = 115\ min)$ correlates to the fraction of remaining material. Another view on the resuspension scenario is given by plotting the fraction remaining against the friction velocity (Figure 9). Starting at a friction velocities lower than $v_{pb}^* < 0.11\ m/s$ the bulk of the graphite particles seem to resuspend between $0.11\ m/s < v_{pb}^* < 0.45\ m/s$ and reaches a rather constant level for larger friction velocities at around $40\%$. Considering single particle resuspension experiments from literature (Hontañón *et al.* (2000), Reeks and Hall (2001)) it was found that $d = 10\ \mu m$ single particles tend to resuspend at friction velocities larger than $0.5$ to $1\ m/s$ and $d = 0.5\ \mu m$ particles start to resuspend at friction velocities larger than $5\ m/s$.
In the present experiment the resuspension seems to begin at much lower friction velocities and approaches a constant plateau at friction velocities of approximately $0.45\ m/s$. The distribution of residual particles in the interspaces of the pebble bed is also visible in the PET-CT overlay after the resuspension scenario at $t = 300\ min$ (Figure 12). Thus, it is assumed that the process observed here was a multilayer resuspension. During the initial deposition phase the injected particles formed multilayer deposits. These structures seem to be resuspended between $0.11\ m/s < v_{pb}^* < 0.45\ m/s$ and the remaining fraction of about $40\%$ can be related to single particles adhering on the pebble surfaces and residual material in the corners recirculation interspaces of the pebble bed. It is assumed that a further increase of the friction velocity up to a value of about $v_{pb}^* > 1\ m/s$ will lead to a further reduction of the residual activity as consequence of additional resuspension of graphite particles from the remote pebble interspaces. Note, the achievable flow rates in the PBLoop were limited by the available power of the radial fans. A doubling of the fluid velocity would require an eight times larger power unit with respect to a constant aerodynamic efficiency. However, these experiments were performed at ambient conditions. It might be of interest, if the resuspension behaviour of a graphite particle multilayer which arose over a long term under thermodynamic conditions similar to the HTR primary circuit might own similar resuspension features. It was observed that graphite particle multilayers undergo a crustification process when being exposed to a high pressure boundary atmosphere (Fachinger *et al.*, 2008).

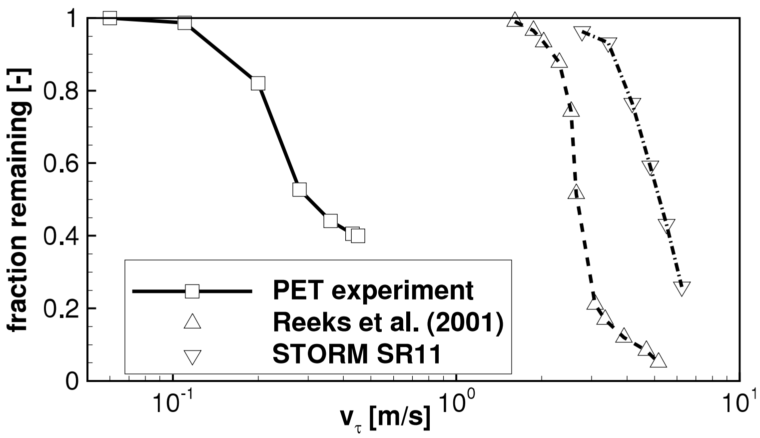


Figure 9 Fraction remaining against friction velocity, solid line: PET data after deposition scenario at $Re_{pb}' = 273$, dotted line: $d = 10\ \mu m$ aluminium particles, dash-dotted line: $d = 0.5\ \mu m$ particles STORM SR11 (Hontañón, et al., 2000)

# 7 Spatial distribution of the reconstructed activity

## 7.1 Longitudinal decay of the particle deposition

The longitudinal distribution of the particle deposits was recorded in terms of the streamwise activity taken by the PET scanner. For this sake, a long term deposition experiment over 6 hours (oil particles, polypropylene spheres) was performed over the 4 tube diameters long pebble bed. The pebble bed was stepwise moved through the FOV in order to acquire the complete longitudinal particle distribution. This distribution is plotted in Figure 10 as slice-wise cumulative intensity, normalized to the maximum value along the pebble bed length. The solid curve is characterized by larger and smaller deviations. The smaller deviations are interpreted as measurement noise of the PET scanner. The larger fluctuations are interpreted as reflecting the inhomogeneous distribution of the particle deposits in the pebble bed. The calculated trend line (dotted line) suggests an exponential decay of the particle deposits in axial direction. Considering the entire pebble bed as a particle filter the exponential downstream decay of particle deposits is similar to the observations of suspended particle concentration over a particle filter by Grahn *et al.* (2010). The below discussed 3D distribution of deposited particles (Figure 11) clearly supports the existence of hot spots of particle deposits in the areas of the upstream stagnation points (front side) of single pebbles. It is assumed that a higher pebble-to-tube diameter ratio would lead to a more homogeneous particle deposition in the pebble bed.

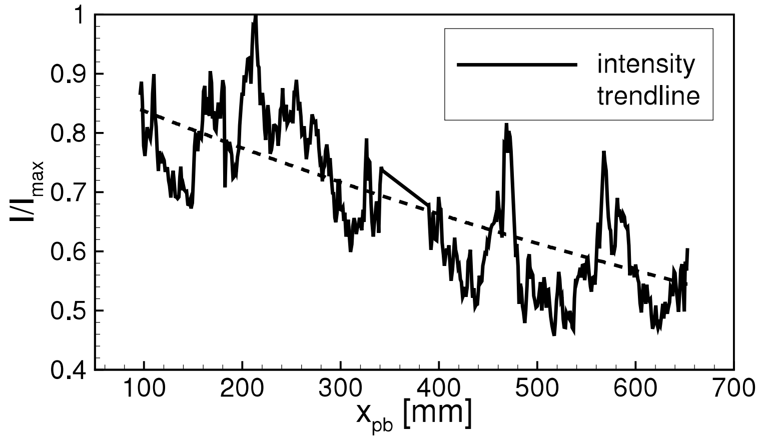


Figure 10 Longitudinal development of PET recorded slice integral intensity

## 7.2 Spatial distribution of the liquid particle deposits

The 3D distribution of liquid particle deposits is reconstructed for a deposition experiment for $d_{aero} = 3.5\ \mu m$ and $Re_p' = 2200$. Figure 11 shows the axial and front views of normalized intensity distributions in the pebble bed. The PET images clearly reveal that the most significant intensity spots are found at the upstream stagnation points of the pebbles. Regarding the radial particle distribution in downstream direction no gravity induced gradient is noticeable. Thus, we conclude that the deposition of the $3.5\ \mu m$ particles at moderately large fluid velocities ($Re_{pb}' = 2200$) is mainly driven by inertia impaction and turbulent dispersion. This effect was already observed in the s-shaped slope of the concentration drop over the pebble bed (Figure 5). At position $(x, y, z) = (20, 80, 90)\ mm$ such a hot spot is clearly visible and even reveals the spherical surface of the pebbles.

Comparing the spatial distribution of particle deposits in the present study with the local temperature distribution published by Hassan (2008) we clearly notice a similarity between the local distributions. Hassan (2008) observed a correlation of the surface temperature of the single pebbles and the formation of the turbulent flow field. Temperature spots were found near the local stagnation points. Considering the activity distribution in the pebble bed after a particle deposition experiment the hot spots are also found in the vicinity of the local stagnation points.

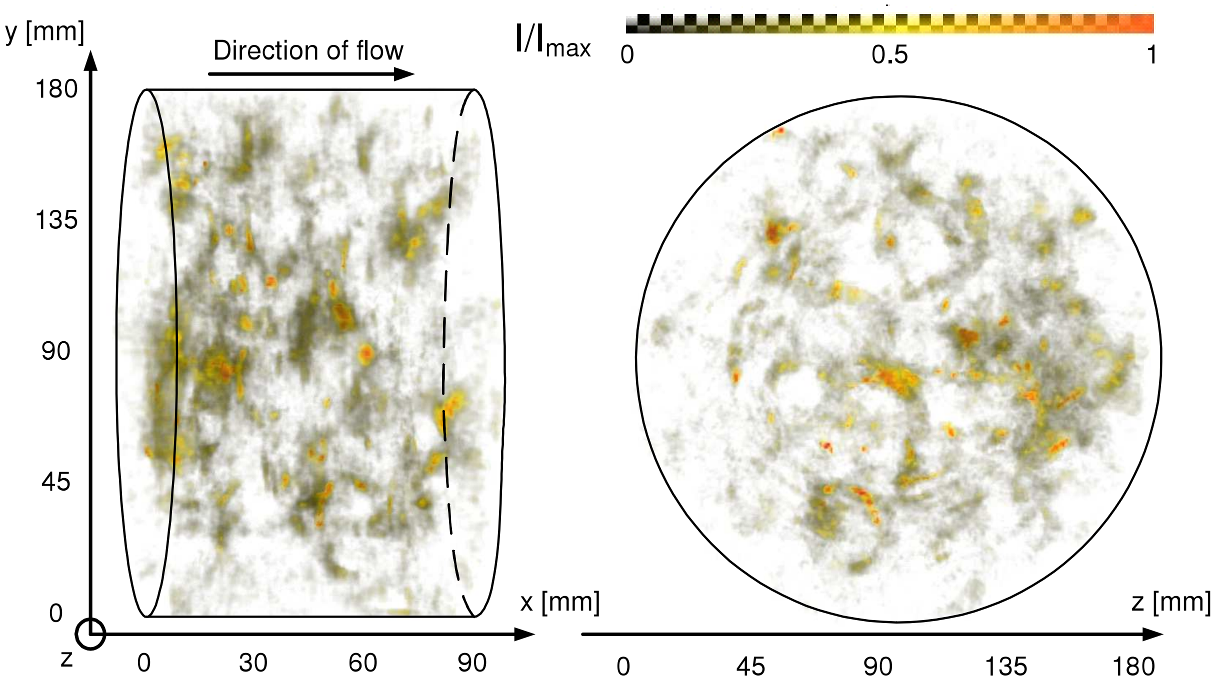


Figure 11 3D image of PET data for deposition experiment $Re_{pb}' = 2200$, $d_{aero} = 3.5\ \mu m$

## 7.3 Spatial distribution of the graphite particle deposits

A time series of PET images was reconstructed during the five phases of the graphite particle experiment as described in section 6.1. 3D image reconstruction requires a data acquisition over approximately 10 minutes to have statistically sufficient events. Therefore, the time step in the set of images is somewhat different from the single phases of the entire campaign. Figure 12 displays a PET-CT overlay of the pebble bed and the reconstructed activity at seven different times. The gravitational vector is oriented in counter y-direction and the flow is oriented along the x-axis. Images $t = 12, 25, 38\ 51$ and $110\ min$ correspond to the deposition phase at which graphite dust was dispersed into the PBLoop at low fluid velocity. The formation of hot spots in the areas of the front side stagnation points of the single pebbles is clearly visible. The hot spots seem to have a slight tendency to the top side of the pebbles indicating the influence of gravitational settling. Passing the pebble bed in downstream/axial direction (not shown here) the slice-wise activity decreases continuously corresponding to the decreasing amount of deposited material in axial direction, which was also observed in the analysis of the slice-wise integral intensity over the pebble bed (Figure 10). The image $t = 123\ min$ shows the reconstructed integral activity of the resuspension scenario (period 4). At this time the better part of the activity hot spots at the front sides of the single pebbles was already removed. The activity seems to distribute more homogeneously over the entire FOV. It can be concluded that the large graphite particle agglomerations have been resuspended and the remaining material distributes in the interspaces of the pebble bed at which the local fluid forces are much lower. The last image denoted as $t = 300\ min$ is an integrated image reconstruction over the final period after the resuspension (period 5). In this image only small activity fractions are visible on the back sides of the pebbles and in the interspaces of the pebble bed close to the tube wall. Note, a lower threshold of $4\ Bq/voxel$ has been chosen in the colour bar to blank measurement noise and to highlight the dominating structures. Changing the lower threshold of the colour bar from $4$ to $1\ Bq/voxel$ remaining activity evenly distributed all over the pebble surfaces appears indicating remaining single particles adhering on the pebble surfaces. This assumption is in consistency to the plot of the fraction remaining against the friction velocity (Figure 9).

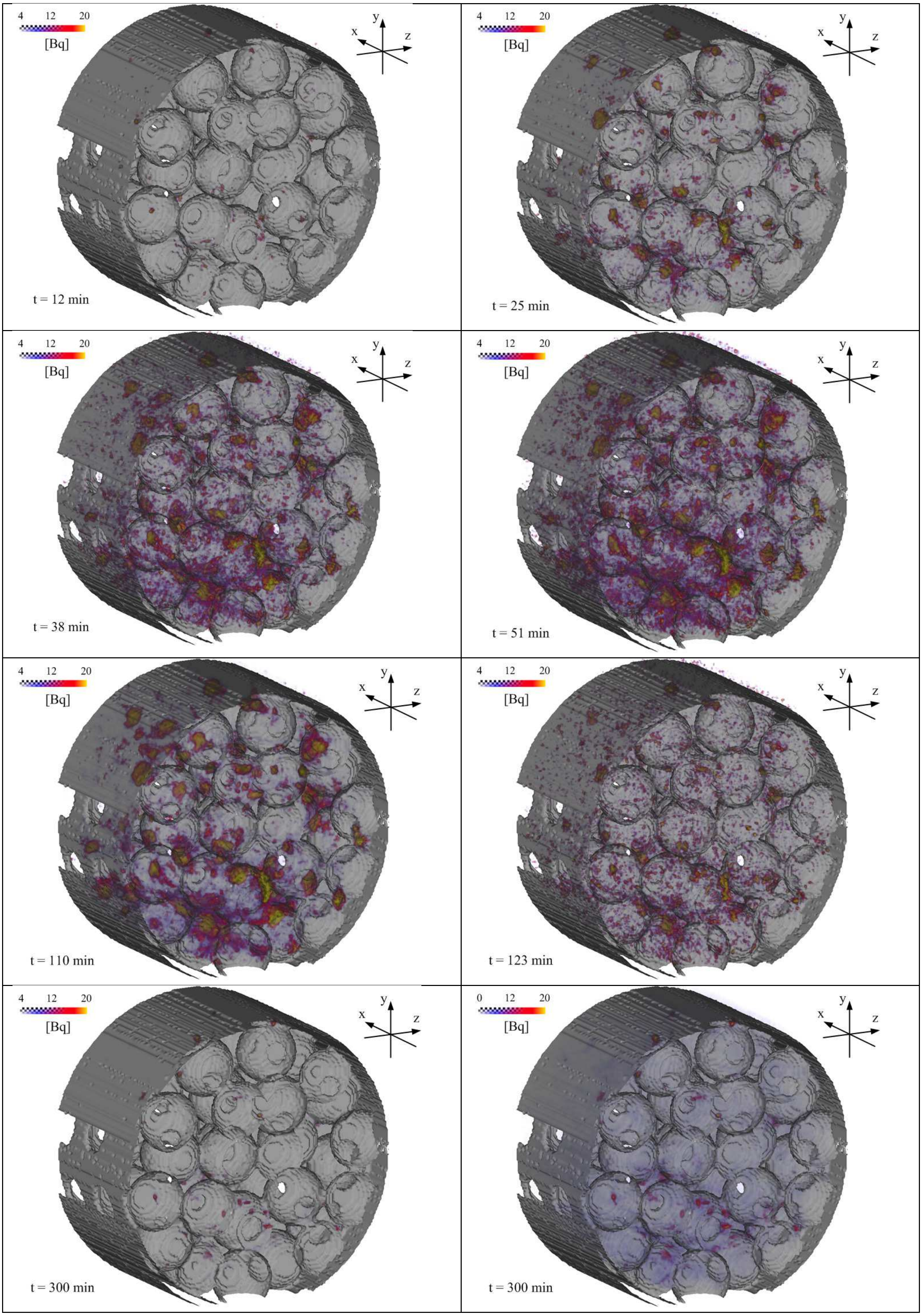


Figure 12 Time series of reconstructed PET-CT overlay of the graphite particle $Re_{pb}' = 273$ experiment

# 8 Summary and outlook

This report describes a set of particle deposition and resuspension experiments in a pebble bed. Background motivation is the safety assessment of pebble bed type HTRs. During reactor operation, carbonaceous dust arises and deposits on the inner surfaces of the primary circuit. Fission product activity in the coolant adheres to the dust particles which may contribute to the source term in case of a Design Basis Accident such as the depressurisation of the primary circuit.

A small-scale test facility was designed to generate a particle laden turbulent flow through a pebble bed. The facility is a closed loop consisting of steel pipes, the pebble bed, a particle filter and a power unit. The flow field was fluid dynamically downscaled from the HTR core flow to a model pebble bed by the Reynolds number. Pressure and velocity measurements have been performed using an inclined tube manometer connected to pressure ports to quantify the flow field. It was found that the total pressure drop over the pebble bed is in good consistency to published data which demonstrates the validity of the fluid dynamic scaling.

Aerosol particles have been used matching the size distribution the graphite dust previously found in former HTR test reactors. In the first experiment, liquid monodisperse oil particles were dispersed into the flow to study pure particle deposition. In the second set of the investigation the oil particles were replaced with technical graphite dust to study particle resuspension. Particle concentration measurements upstream and downstream of the pebble bed were done to determine the particle number and mass concentration, respectively. A particle laden air sample was taken isokinetically by a Pitot tube shaped sampling nozzle and was guided to an out-stack sampling station. The number concentration of the liquid particles was recorded by a condensational particle counter. The aerodynamic particle size distribution was measured by an Aerodynamic Particle Sizer and the graphite particle mass concentration was recorded by filter measurements. The particle concentration drop over the pebble bed was studied with respect to particle size and fluid velocity. It was found that the deposition rate considerably increases with growing particle size and fluid velocity indicating that the particle deposition is mainly driven by turbulent dispersion and inertia impaction.

The geometry of the pebble bed was obtained from a gamma ray computed tomography scan (CT). The CT data was used to provide a full 3D geometry for a final overlay with the PET data. Two different sets of PET experiments have been performed. Firstly, monodisperse liquid particles were dispersed into the facility to study pure particle deposition over a wide particle size flow velocity range. It was found that the count rates of the PET scanner constantly increase with time indicating a constant particle deposition rate over the pebble bed. The axial decay of the particles was evaluated in terms of the integral slice intensity in mean flow direction. Most of the particles deposit within the first pebble packing and further downstream the particle material decreases exponentially. The 3D distribution of the particle deposits was reconstructed out of a PET measurement for rather large fluid velocities and particle sizes. The particles form spots on the front sides of the single pebbles supporting the thesis of inertia driven particle deposition.

In the second set of experiments, the liquid particles were replaced with technical graphite dust. Similarities between the two experiments were found. For instance, the count rates during a pure deposition experiment also show a linear uptake with time indicating a constant particle deposition flow rate into the pebble bed. After the particle deposition experiment, the aerosol generator was switched off and the fan power was stepwise increased to induce particle resuspension. The PET scanner instantly detected a drop in the count rates when a critical friction velocity has been exceeded indicating immediate remobilisation of the deposited graphite particles. Comparing the normalized count rates to literature data shows that the resuspension of the present multilayer deposits starts to remobilise at friction velocities smaller than the necessary pull off velocities for single particle resuspension. Note, the present count rates approach a plateau of approximately *40%* of the initial count rates revealing the thesis of particle multilayer resuspension. The large particle spots at the front sides of the pebbles have been removed and only residual single particles remaining in the pebble bed. A fully 3D PET CT overlay of one campaign was present. The formation of particle spots during a pure deposition regime and the removal of these particle deposits during the resuspension transient were clearly visible.

In summary, the two sets of experiments provide a data basis for CFD code development to compute the particle deposition and resuspension within a HTR type pebble bed. The first set of experiments provides data about the total pressure drop against the pebble bed Reynolds number. The results of the particle concentration measurements give an indication about the overall particle deposition behaviour with respect to particle size and fluid velocity. The 3D PET-CT overlay gives a spatiotemporal insight into the formation of particle deposits in the pebble bed. The second set of experiments provides a fully 3D and time resolved insight into the particle deposition and the resuspension during flow transients. In the future, it is of interest to further develop the experimental facility in order to get closer to the HTR relevant thermal fluid boundary conditions. The air-driven closed loop may be upgraded to a pressurized Helium loop equipped with a heating system to study the influence of temperature.

# 9 References


Eisfeld, B., & Schnitzlein, K. (2001). The influence of confining walls on the pressure drop in packed beds. *Chemical Engineering Science,* **56**, 4321-4329.

Fachinger, J., von Lensa, W., & Podruhzina, T. (2008). Decontamination of nuclear graphite. *Nuclear Engineering and Design,* **238**, 3086 - 3091.

Farnsworth, J.E., & Caldow, R. (2010). A method for empirical measurement of CPC upper-end counting efficiency. In (Edited Editor), *Book A method for empirical measurement of CPC upper-end counting efficiency*, City.

Grahn, A., Krepper, E., Weiss, F.-P., Alt, S., Kastner, W., Kratzsch, A., & Hampel, R. (2010). Implementation of a Pressure Drop Model for the CFD Simulation of Clogged Containment Sump Strainers. *Journal of Engineering for Gas Turbines and Power,* **132**, 082902.

Hampel, U., Bieberle, A., Hoppe, D., Kronenberg, J., Schleicher, E., Suhnel, T., Zimmermann, F., & Zippe, C. (2007). High resolution gamma ray tomography scanner for flow measurement and non-destructive testing applications. *Rev Sci Instrum,* **78**, 103704.

Hassan, Y.A. (2008). Large eddy simulation in pebble bed gas cooled core reactors. *Nuclear Engineering and Design,* **238**, 530 - 537.

Hassan, Y.A., & Dominguez-Ontiveros, E.E. (2008). Flow visualization in a pebble bed reactor experiment using PIV and refractive index matching techniques. *Nuclear Engineering and Design,* **238**, 3080–3085.

Hontañón, E., de los Reyes, A., & Capitão, J.A. (2000). THE CÆSAR CODE FOR AEROSOL RESUSPENSION IN TURBULENT PIPE FLOWS. ASSESSMENT AGAINST THE STORM EXPERIMENTS. *Journal of Aerosol Science,* **31**, 1061 - 1076.

Levin, C.S., & Hoffman, E.J. (1999). Calculation of positron range and its effect on the fundamental limit of positron emission tomography system spatial resolution. *Phys Med Biol,* **44**, 781-799.

Peters, T.M., & Leith, D. (2004). Particle Deposition in Industrial Duct Bends. *Annals of Occupational Hygiene,* **48**, 483-490.

Phelps, M.E. (2006). *Pet: Physics, Instrumentation, And Scanners*. Springer.

Pope, S.B. (2009). *Turbulent Flows*. Cambridge University Press.

Reeks, M.W., & Hall, D. (2001). Kinetic models for particle resuspension in turbulent flows: theory and measurement. *Journal of Aerosol Science,* **32**, 1 - 31.

Rott, & Wahsweiler. (1991). *Auswertung von Inbetriebnahmeergebnissen am THTR-300 für HTR-Nachfolgeanlagen: Nachuntersuchungen von THTR-Betriebselementen(BTE); Berichtszeitraum: 01.02.1989- 30.06.1991*. Hochtemperatur-Reaktorbau GmbH.

Sempere-Roldan, P., Chereul, E., Dietzel, O., Magnier, L., Pautrot, C., Rbah, L., Sappney-Marinier, D., Wagner, A., Zimmer, L., Janier, M., Tarazona, V., & Dietzel, G. (2006). Raytest ClearPET, a new generation small animal PET scanner. *Nuclear Instruments and Methods in Physics Reasearch,* **571**, 498-501.

Thielemans, K., Tsoumpas, C., Mustafovic, S., Beisel, T., Aguiar, P., Dikaios, N., & Jacobson, M.W. (2012). STIR: software for tomographic image reconstruction release 2. *Phys Med Biol,* **57**, 867-883.

Truckenbrodt, E. (2008). *Fluidmechanik Band 1 - Grundlagen und elementare Strömungsvorgänge dichtebeständiger Fluide* (4. Auflage ed.). Springer Berlin / Heidelberg.

Vincent, J.H. (2007). *Aerosol sampling: science, standards, instrumentation and applications*. John Wiley \& Sons.

Ziermann, E., & Ivens, G. (1997). Abschlussbericht ueber den Leistungsbetrieb des AVR-Versuchskraftwerkes. In (Edited Editor), *Book Abschlussbericht ueber den Leistungsbetrieb des AVR-Versuchskraftwerkes*. Forschungszentrum Juelich, City.